# Effects of Process Parameters upon the Shape Memory and Pseudo-Elastic Behaviors of Laser-Welded NiTi Thin Foil

C.W. CHAN, H.C. MAN, and T.M. YUE

This article discusses the effects of laser welding parameters such as power, welding speed, and focus position on the weld bead profile, microstructure, pseudo-elasticity (PE), and shape memory effect (SME) of NiTi foil with thickness of 250 $\mu$m using 100W CW fiber laser. The parameter settings to produce the NiTi welds for analysis in this article were chosen from a fractional factorial design to ensure the welds produced were free of any apparent defect. The welds obtained were mainly of cellular dendrites with grain sizes ranging from 2.5 to 4.8 $\mu$m at the weld centerline. A small amount of $Ni_3Ti$ was found in the welds. The onset of transformation temperatures ($A_s$ and $M_s$) of the NiTi welds shifted to the negative side as compared to the as-received NiTi alloy. Ultimate tensile stress of the NiTi welds was comparable to the as-received NiTi alloy, but a little reduction in the pseudo-elastic property was noted. Full penetration welds with desirable weld bead profiles and mechanical properties were successfully obtained in this study.

## I. INTRODUCTION

THE use of Nitinol (NiTi) in the implantable medical device industry has been widely recognized because of its unique shape memory effect (SME) and pseudo-elasticity (PE).[1–4] A typical example of the implantable medical devices are electrical stimulator implants for skeletal muscles and pacemakers. Devices such as radio frequency (RF)-powered implants with antenna displacement dependent stimulation, RF-powered implants with stabilized stimulation amplitude, and battery powered implants are all concerned with hermetic metal case welding and connections of electrical conductors.[5–7] Although the microstructural mysteries of shape memory NiTi were solved by metallurgists since 1970s, product engineers still find great difficulties in understanding nonlinear tensile properties, hysteresis, fatigue, and adiabatic heating and cooling effects of NiTi alloy.[2] One of the major challenges for product engineers to use NiTi as the material for medical devices is the joining of NiTi, because significant changes in structural properties of SME and PE could have resulted after the joining process.

In recent years, there are increasing attempts to perform laser microwelding for medical devices made of stainless steel or NiTi. Laser microwelding provides high precision and localized heat input as compared to other conventional joining methods. Fuerschbach and Hinkley[8] studied laser welding of cardiac pacemaker batteries with reduced heat input. Anon[9] pointed out some major characteristics of precision laser microwelding of medical devices. Yoneyama et al.[10] listed a number of applications of NiTi alloy in the dental field, which made use of the desirable SME and PE properties. The applications include orthodontic arch wires, coil springs, expansion appliance, flexible root canal files, and dental castings. Sevilla et al.[11] showed the possibility of applying the laser welding on different commercial NiTi orthodontic wires. They provided a detailed report on the mechanical properties, phase transformation, corrosion resistance, and biocompatibility of the laser-welded NiTi orthodontic welded wires.

Most studies on laser welding of shape memory NiTi alloy mainly made use of Nd:YAG lasers, and the process of parameter optimization was rarely discussed.[11–18] In this study, a fiber laser, which has a smaller beam size and higher power intensity than a normal Nd:YAG laser, was used to weld thin NiTi foil of 0.25-mm thickness. The inter-related effects of laser parameters, power input, welding speed, and focus position on the weld bead profiles and microstructures, as well as pseudo-elastic, shape memory, and mechanical properties, were investigated by the fractional factorial (or Taguchi) design approach.

C.W. CHAN, Research Student, H.C. MAN, Professor and Head of Department, and T.M. YUE, Professor, are with the Laser Processing Group, Advanced Manufacturing Technology Research Centre, Department of Industrial and Systems Engineering, The Hong Kong Polytechnic University, Hunghom, Kowloon, Hong Kong, P.R. China. Contact e-mail: mfhcman@polyu.edu.hk
Manuscript submitted June 24, 2010.
Article published online February 17, 2011.

## II. EXPERIMENTAL DETAILS

The material used was annealed Ti-55.91 wt pct Ni foil in the form of 50 × 50 × 0.25 mm. It was cut into pieces of 10 × 10 × 0.25 mm, and the surfaces were ground clean using 600 grit SiC papers. Bead-on-plate weld tracks were performed on each piece of the NiTi

foil. A 100 W CW fiber laser (SP-100C-0013) with an output wavelength of 1091 nm was adopted for this investigation. The beam was focused using a focal lens with a 91-mm focal length. By using a sloping welding track technique, the best focus position was found to be 89.8 mm. The theoretical focused spot size was calculated to be 46 $\mu$m using the formula in Reference 19.

The laser beam was kept stationary and the specimens were traversed with a CNC X-Y table. In order to minimize the contamination of oxygen, hydrogen, and nitrogen in the weld zone, the welding process was performed using argon shielding. Argon shielding for the underbead was also used. The parameter settings adopted in this study are given in Table I. The parameter settings used to produce the NiTi welds for analysis in this article are indicated by the abbreviation "Ar," which means the samples are welded under the argon shielding environment. The number after the abbreviation "Ar" is the sequence of parameter combinations in the fractional factorial experimental design. There are a total of 27 parameter combinations in the fractional factorial experiment, and eight of them (Ar1, Ar3, Ar7, Ar9, Ar19, Ar21, Ar25, and Ar27) are selected for the in-depth parameter study in this article.

Cross-sectional microstructural study on the weld beads was performed using a scanning electron microscope and optical microscope. The composition was analyzed by energy dispersive X-ray (model JSM-6490, JEOL USA, Peabody, MA). A Bruker D8 Discover diffractometer (Bruker Axs Inc., Madison, WI) was used for X-ray diffraction (XRD) analysis and the parameters were set at 40 kV and 40 mA using Cu $K_{\alpha}$ radiation. A Perkin Elmer DSC 7 system (Waltham, MA) was used for differential scanning calorimetry (DSC) experiment to measure the thermal transformation. Each sample with a mass of 10 to 20 mg was heated in the range of 223 K to 333 K (–50 °C to 60 °C) at 10 °C/min. At 333 K (60 °C), the samples were held for 20 minutes to establish thermal equilibrium. Then the samples were cooled to 223 K (–50 °C) with a cooling rate of 10 °C/min. The phase transformation temperatures were recorded in terms of austenite start temperature ($A_s$), austenite finish temperature ($A_f$), martensite start temperature ($M_s$), and martensite finish temperature ($M_f$). The microhardness of the weld zone was assessed by a Vickers microhardness tester (Shimadzu Seisakusho

NT-M001, Shimadzu Seisakusho Ltd., Kyoto, Japan) at a load of 200 g. An INSTRON* tensile test machine

---

---

was used to carry out the stress-strain measurement at a strain rate of 0.003 mm/s. The samples were individually loaded and unloaded to the elongations of 4, 6, and 8 pct, respectively, and the residual strain for each elongation was recorded to determine the PE. The reduced width and gage length of the tensile testing samples for stress-strain measurement are 4 and 20 mm, respectively.

## III. RESULTS AND DISCUSSION

### A. *Effects of Process Parameters upon the Weld Bead Dimensions*

The weld bead profiles of laser welding are strongly affected by the total heat input, rate of heat input, power intensity, energy coupling efficiency as well as rate of heat loss, and thermal capacity of the material.[20] The dimensions of the weld profiles obtained in this work are listed in Table II and shown in Figure 1. It can be seen in Figure 1 that with increasing power input–to–welding speed (P/V) ratio, the weld bead cross-sectional profile changed from hemispherical to triangular and then to

Table II.  Dimensions of Welds Ar 1 to Ar 27

| TC | Width ($\mu$m), $w$ | Penetration ($\mu$m), $d$ | Aspect Ratio, $d/w$ | Power-to-Speed Ratio (W mm$^{-1}$ min), P/V |
|---|---|---|---|---|
| Ar1 | 689 | 250 | 0.36 | 21.0 |
| Ar3 | 652 | 250 | 0.38 | 21.0 |
| Ar7 | 481 | 178 | 0.37 | 12.6 |
| Ar9 | 415 | 162 | 0.39 | 12.6 |
| Ar19 | 851 | 250 | 0.29 | 25.7 |
| Ar21 | 734 | 250 | 0.34 | 25.7 |
| Ar25 | 642 | 250 | 0.39 | 15.4 |
| Ar27 | 588 | 250 | 0.43 | 15.4 |
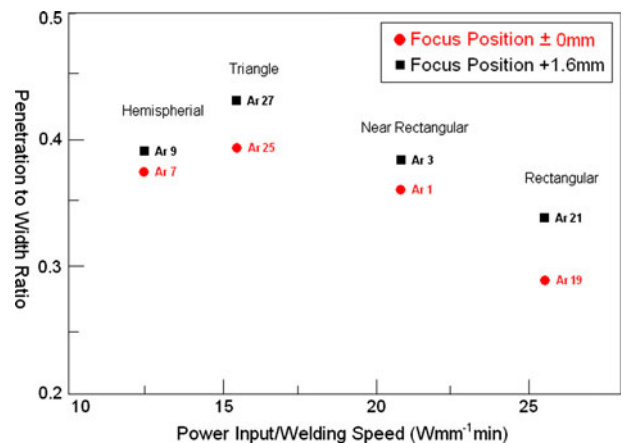


Fig. 1—Aspect ratio *vs* power input to welding speed (P/V) ratio.

Table I.  Parameter Combinations from the Fractional Factorial Experimental Design

| TC | Power Input (W), P | Welding Speed (min$^{-1}$ mm), V | Focus Position (mm) |
|---|---|---|---|
| Ar1 | 63 | 180 | ±0 |
| Ar3 | 63 | 180 | +1.6 |
| Ar7 | 63 | 300 | ±0 |
| Ar9 | 63 | 300 | +1.6 |
| Ar19 | 77 | 180 | ±0 |
| Ar21 | 77 | 180 | +1.6 |
| Ar25 | 77 | 300 | ±0 |
| Ar27 | 77 | 300 | +1.6 |

near rectangular, which is the profile of fully penetrated welds. The changes of cross-sectional profiles correspond to the changes of mode of heat transfer from conduction mode to keyhole mode. In order to minimize heat distortion to the parts, it is desirable to effect completing melting as quickly as possible. Hence, it is always desirable to couple the laser energy into the materials *via* the keyhole mechanism. When the P/V ratio reaches a critical value, laser energy is coupled into the material *via* the keyhole mechanism and more material is able to be melted. If the material is a few millimeters thick, heat transfer along the depth dimension would be the quickest and a keyhole shape of weld bead would have resulted. However, as the material in this work is only 0.25-mm thick, the energy therefore is used to melt the materials along the width of the weld. Hence, a rectangular cross section is formed. This is more desirable in thin foil welding as this will reduce the risk of having undercuts in which a weld gap might exist in between the welding pairs.

## B. *Effects of Process Parameters on the Weld Microstructure*

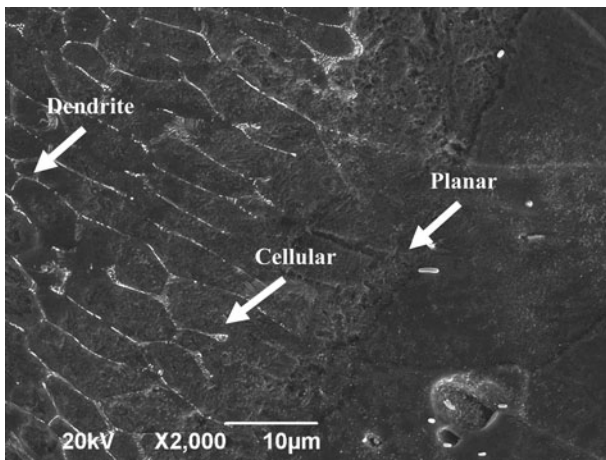The solidification microstructure of the fusion zone depends on the parameters of temperature gradient ($G$),



Fig. 2—Morphology transition in the NiTi weld.

growth rate ($R$), undercooling ($\Delta T$), and alloy composition. The ratio $G/R$ determines the mode of solidification, and the combined form $GR$ (cooling rate) influences the size of solidification structure.[20] The solidification mode changes from planar to cellular and from cellular to dendritic when constitution supercooling increases.

As shown in Figure 2, the solidification mode across the fusion zone changed from planar to cellular and cellular to dendritic because of the increase in cooling rate from the weld zone interface toward the centerline. When the solidification front approaches the weld centerline, the growth rate reaches its maximum as the temperature gradient is at its minimum. As shown in Figure 2, the cellular grains grew epitaxially from the interface and followed the easy-growth direction {110} of the parent NiTi grain. The grain structure at the interfacial zone was determined by the base metal grain structure and the welding conditions, because the solidification of the weld metal begins spontaneously by epitaxial growth of the partially melted grains in the base metal.

Figure 3 shows the XRD patterns of the as-received NiTi and the welded beads. The {110} and {211} peaks of the austenitic B2 phase were observed in all specimens. Besides the B2 phase, a $Ni_3Ti$ peak with low intensity was observed in the XRD pattern of the welds. It is of interest to note that, for the welds with lower P/V ratio, *i.e.*, specimens Ar7 and Ar9, the grains grew along the easy growth {110} direction as a result of higher cooling rate, and nearly no {211} peak was detected.

The size of cellular dendrites was affected by the process parameters, and a size range of 2.5 to 4.8 $\mu$m was found at the weld centerline because of the highest cooling rate in this region. The solidification mode is significantly affected by the power input and welding speed. Under the same welding speed, the $G/R$ ratio decreases with increasing power input because of the lower temperature gradient ($G$). The cell spacing decreases with increasing cooling rate. The cooling rate increases with decreasing power input and welding speed ratio. The grains were finer at higher welding speed (300 min$^{-1}$ mm) and low power input (63 W), while the grains became coarser when power input was increased (77W) and welding speed reduced (180 min$^{-1}$ mm). Furthermore, the welding
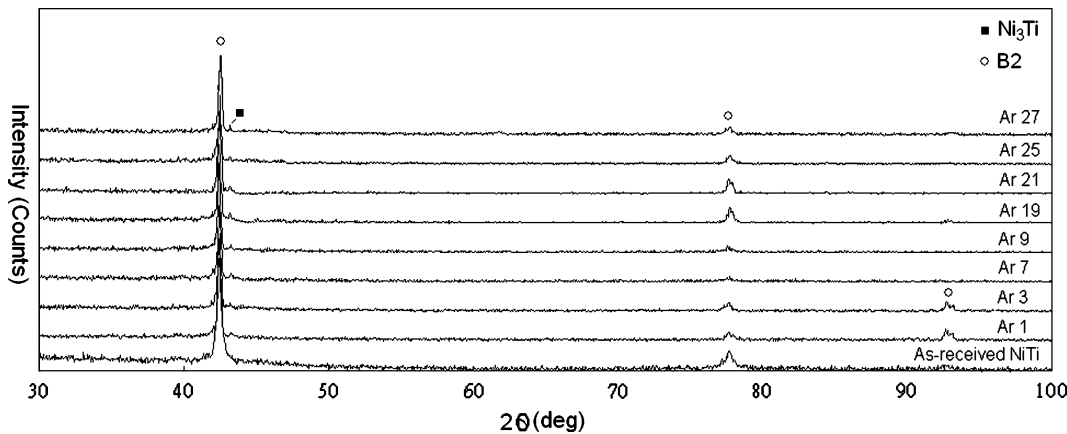


Fig. 3—XRD patterns of the as-received NiTi alloy and the NiTi welds.

speed was found to be the predominantly important factor that governs the formation of finer grains as compared to power and focus position. Focus position was least important to the cell spacing in both the fusion zone and heat-affected zone (HAZ) in fiber laser welding. The cell spacing in the HAZ was, on average, 5 times larger than that in the weld centerline.

## C. Effects of Parameters on the Phase Transformation

Figures 4(a) and (b) show the DSC curves of the as-received and welded NiTi at different welding parameter combinations. As shown in the figure, the as-received NiTi exhibited one endothermic peak (B2 to B19') and one exothermic peak (B19' to B2) during heating and cooling. No R phase appeared prior to the martensitic transformation. This one-step transformation is a typical behavior of a fully annealed NiTi alloy.
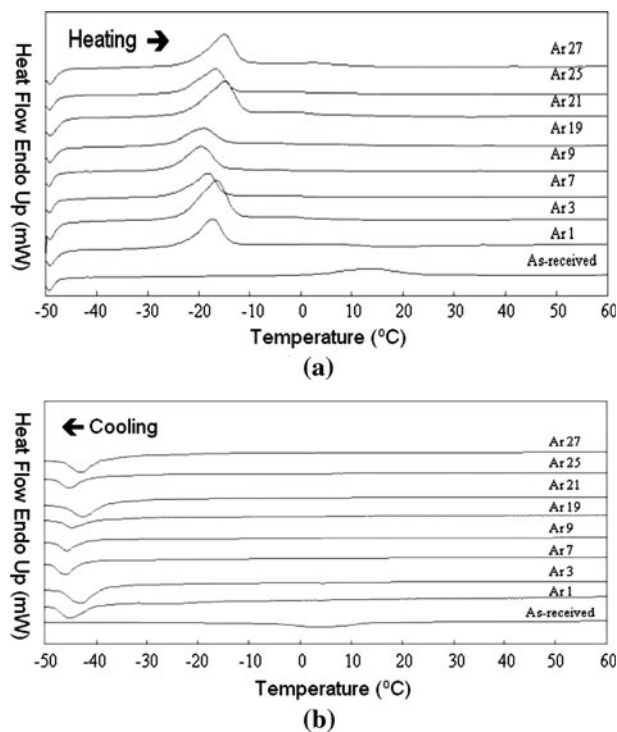


Fig. 4—(a) DSC heating curves for the as-received and laser-welded NiTi samples. (b) DSC cooling curves for the as-received and laser-welded NiTi samples.

The laser-welded samples also exhibited one-step transformation upon heating and cooling. The transformation temperature only changed a little for welds made with different welding parameter combinations used in this study. The $A_s$ point and the $M_s$ point lie in the range of 250.6 K to 247.2 K (–22.4 °C to –25.8 °C) and 235.8 K to 233.5 K (–37.2 °C to –39.5 °C), respectively. Compared to the as-received NiTi, the onset of transformation temperatures, $A_s$ and $M_s$, of the welded samples changed abruptly from 276.8 K to 249.6 K (3.8 °C to –23.4 °C) and 285 K to 234.6 K (12 °C to –38.4 °C) in average, respectively. The transformation temperatures, $A_s$, $A_f$, $M_s$, $M_f$, of the as-received and welded samples are summarized in Table III. Additionally, the transformation peaks of the welded samples became sharper than those of the as-received NiTi.

The remarkable decrease in the austenite and martensite transformation temperatures was attributed to the thermally induced defects in the weld microstructure.[21] The resolidification of material during laser welding alters the microstructure, chemical composition, and grain size in the weld zone. First, the precipitation of $Ni_3Ti$ particles surrounding the B2 phase changes the local Ni content and, hence, the Ni distribution in the weld zone. It has been reported that the austenite and martensite transformation temperatures are highly correlated with the Ni/Ti ratio.[22–27] Therefore, little change in the Ni/Ti ratio in the weld zone would considerably affect the transformation temperatures. Second, the increase in grain size decreases the amount of nucleation sites for the martensitic B19' phase in the weld zone and, thus, alters the transformation temperatures during the phase transformation process. Finally, the precipitation of the intermetallic phases and variations of the microstructure and grain size in the weld zone create lattice dislocations that result in the increase of residual stress in the alloy after laser welding. Such thermally induced changes in the NiTi matrix could lower the transition temperature, because those defects created by laser welding would act to inhibit martensite transformation by hindering the phase reorientation process.[26] Also, the presence of the containments such as oxygen, hydrogen, and nitrogen in the fusion zone also affect the SME.

## D. Mechanical and Pseudo-Elastic Properties

Figure 5 shows the tensile stress-strain curve of the full penetration weld Ar25 and the as-received NiTi.

Table III. Transformation Temperatures of the NiTi Samples

| TC | $A_s$ [K (°C)] | $A_f$ [K (°C)] | $M_s$ [K (°C)] | $M_f$ [K (°C)] |
|---|---|---|---|---|
| As-received | 269.2 (3.8) | 249.5 (23.5) | 263.0 (12.0) | 268.9 (–4.1) |
| Ar1 | 250.5 (–22.5) | 259.6 (–13.4) | 234.6 (–38.4) | 225.5 (–47.5) |
| Ar3 | 250.0 (–23.0) | 259.9 (–13.1) | 235.3 (–37.7) | 226.2 (–46.8) |
| Ar7 | 247.8 (–25.2) | 258.0 (–15.0) | 233.8 (–39.2) | 224.5 (–48.5) |
| Ar9 | 247. 2 (–25.8) | 257.8 (–15.2) | 233.5 (–39.5) | 225.0 (–48.0) |
| Ar19 | 250. 4 (–22.6) | 260.1 (–12.9) | 235.3 (–37.7) | 225.7 (–47.3) |
| Ar21 | 251.6 (–22.4) | 260.4 (–12.6) | 235.8 (–37.2) | 226.4 (–46.6) |
| Ar25 | 249.7 (–23.3) | 260.3 (–12.7) | 234.3 (–38.7) | 225.1 (–47.9) |
| Ar27 | 250.3 (–22.7) | 260.0 (–13.0) | 234.4 (–38.6) | 225.9 (–47.1) |
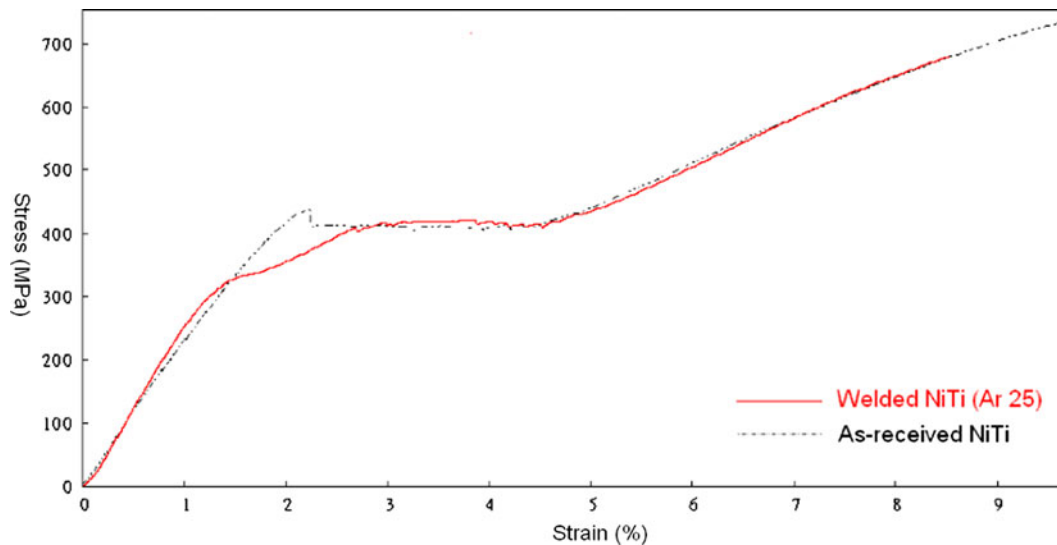
Fig. 5—Stress-strain curves of the as-received and laser-welded NiTi samples.

The first yielding of the as-received NiTi occurs at the stress value of 420 MPa, which is the starting point of the deformation due to stress induction of the B19' martensite from the B2 phase. A stress plateau followed by the apparent yield point represents the detwinning deformation process. This stress-induced B19' martensite gives rise to a strain of 2.1 pct. A sharp increase in the stress due to the elastic deformation of the martensitic structure is observed after the stress plateau. Fracture eventually occurred at the stress value of 730 MPa with a strain of 9.5 pct. The stress-strain curve of the welded sample Ar25 basically followed the same path as the as-received NiTi; however, the clear onset of the yielding point, which denotes the detwinning deformation, disappeared and was replaced by a smooth transition from the first yielding to the stress plateau. The ultimate tensile stress of the welded sample was 95 pct of the as-received NiTi, which was about 690 MPa with a strain of 8.8 pct. The stress plateau of the welded NiTi was reduced from 2.1 to 1.7 pct. The reduction in the stress plateau is believed to be the result of dislocation, which occurred within the grains because of the inhomogeneity in the grain structure among the fusion zone, HAZ, and base metal.[13,15,28]

The pseudo-elastic behavior of the welded and as-received NiTi was studied by examining the residual strain in loading and unloading the samples at various strains of 4, 6, and 8 pct, respectively. The samples were heated to 323 K (50 °C) before the tensile test, ensuring complete transformation of austenite B2 phase to actuate the pseudo-elastic property. Figure 6(a) shows the pseudo-elastic behavior of the as-received NiTi. As seen in the figure, the as-received NiTi showed residual strains of 0.4, 0.9, and 1.3 pct when loading and unloading at elongations of 4, 6, and 8 pct, respectively. Compared to the as-received NiTi, the welded sample showed little reduction in the pseudo-elastic property; the residual strains were recorded as 0.8, 1.2, and 1.7 pct for 4, 6, and 8 pct elongations, respectively (Figure 6(b)). The residual strains of the as-received and welded NiTi
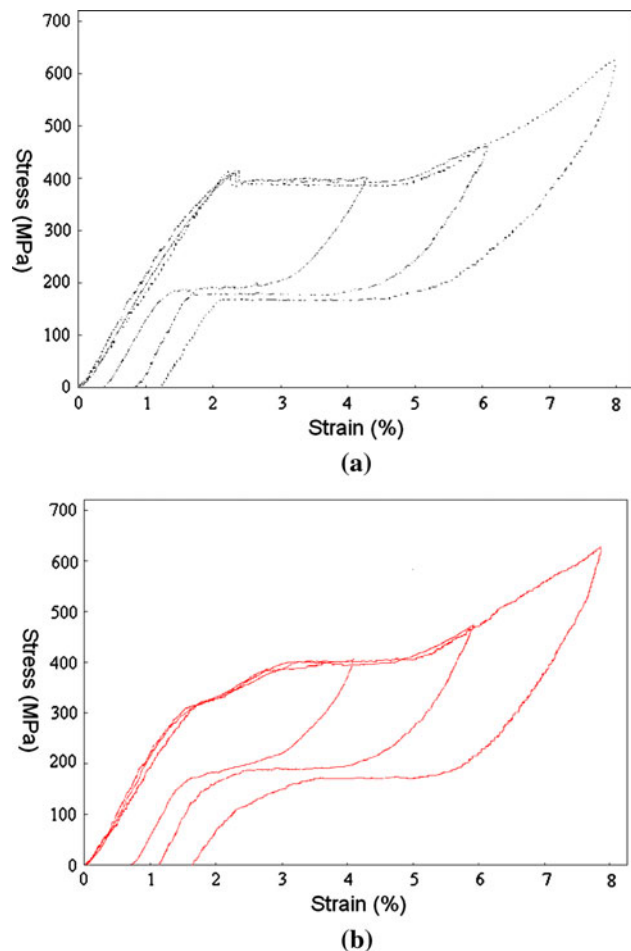


Fig. 6—(a) Stress-strain curves of as-received NiTi sample with 4, 6, and 8 pct elongations. (b) Stress-strain curves of laser-welded NiTi sample with 4, 6, and 8 pct elongations.

for the 4, 6, and 8 pct elongations are summarized in Table IV. The increase in the residual strain was probably due to the existence of a small amount of

**Table IV. Residual Strain of the As-Received and Laser-Welded NiTi Samples**

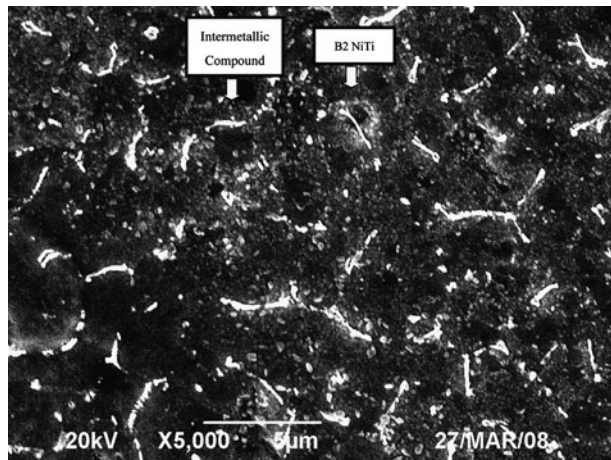| Elongation | 4 Pct | 6 Pct | 8 Pct |
|---|---|---|---|
| As-received NiTi | 0.4 pct | 0.9 pct | 1.3 pct |
| Laser-welded NiTi | 0.8 pct | 1.2 pct | 1.7 pct |



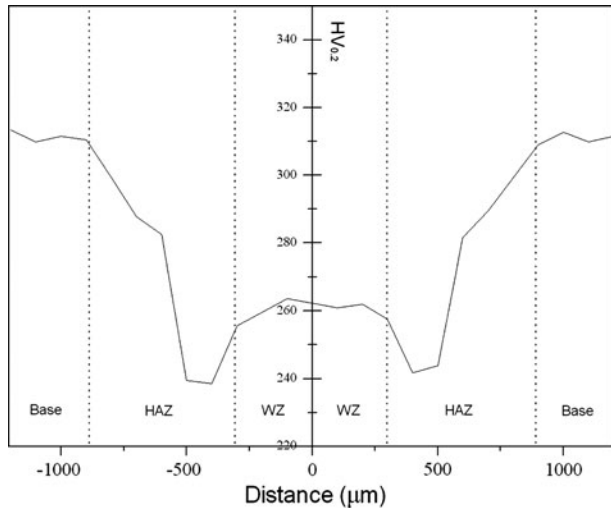Fig. 7—Intermetallic compound around the B2 NiTi grain boundary.



Fig. 8—Microhardness in the fusion zone, HAZ, and base metal of laser-welded NiTi sample.

intermetallic compound formed at the NiTi grain boundary in the fusion zone, as shown in Figure 7, which hindered the reorientation of martensite, and therefore weakened the PE. The fairly good PE of the as-received NiTi was attributed to the homogeneous microstructure and chemical composition.

It is believed that the mechanical and structural properties of NiTi alloy are primarily affected by the transformation behavior and phase structure of the alloy. As confirmed by DSC and XRD analyses, no significant change in the phase structure and transformation temperatures is observed between the welds produced by different parameter combinations. Therefore, it is expected that the properties of NiTi weld would not be improved by only changing the process parameters, given the existence of thermally induced defects caused by laser welding. Postweld heat treatment should be applied on the laser-welded NiTi alloy to modify the phase structure and to relieve the thermal residual stress in the weld zone, and hence to improve the mechanical and structural properties of the NiTi weld.[29]

### E. Microhardness

The microhardnesses across the fusion zone, HAZ, and base metal are measured and shown in Figure 8. As described in Figure 8, the microhardness values in the fusion zone and base metal were fairly constant at 265 and 310 $HV_{0.2}$, respectively. It is of particular interest to note that the microhardness in HAZ initially is reduced and reached its minimum point of 240 $HV_{0.2}$ at a distance of 500 $\mu$m away from the center of the fusion zone. Then, the microhardness sharply increased and attained its highest point at 800 $\mu$m away from the fusion zone center. This clear transition in microhardness value was due to the change of the grain structure in the HAZ. A finer grain structure was observed at the side near the base metal, while the grain near the fusion zone was coarser. The base metal showed the highest value of microhardness because of the chemical and microstructural homogeneity.

## IV. CONCLUSIONS

In this study, the effects of fiber laser welding parameters on the weld bead profile, microstructure, SME, and PE, as well as the mechanical properties of Ni-rich NiTi foil, were investigated. Full penetration welds for the 0.25-mm thin NiTi foil could be obtained when the power input to welding speed ratio was higher than 15.4 W mm$^{-1}$ min.

Besides the NiTi matrix phase of B2, a small amount of $Ni_3Ti$ was detected in the welds. The onset of transformation temperatures ($A_s$ and $M_s$) of the welds shifted to the very negative side as compared with the as-received NiTi. The change of welding parameters only induced a small variation in the transformation temperatures. A small reduction in the pseudo-elastic property was observed in the laser-welded foil. A 5 pct drop in the ultimate tensile stress was noted in the laser-welded foil as compared with the as-received foil. A significant decrease of the microhardness of the weld zone was observed.

# REFERENCES

1. G.R. Purdy and J.G. Parr: *Trans. AIME*, 1981, vol. 2, pp. 23–25.
2. T. Duerig, A. Pelton, and D. Stockel: *Mater. Sci. Eng. A*, 1999, vols. 273–275, pp. 149–60.
3. T. Duerig, D. Stockel, and D. Johnson: *Proc. SPIE 4763,* 2003, pp. 7–15.
4. N.B. Morgan: *Mater. Sci. Eng. A*, 2004, vol. 378, pp. 16–23.
5. R.G. Dennis, D.E. Dow, and J.A. Faulkner: *Med. Eng. Phys.*, 2003, vol. 25, pp. 239–53.
6. H. Lanmuller, Z. Ashley, E. Unger, H. Sutherland, M. Reichel, M. Russold, J. Jarvis, W. Mayr, and S. Salmons: *Med. Bio. Eng. Comp.*, 2005, vol. 43, pp. 535–40.
7. P.H. Peckham and J.S. Knutson: *Annu. Rev. Biomed. Eng.*, 2005, vol. 7, pp. 327–60.
8. P.W. Fuerschbach and D.A. Hinkley: *Weld. J.*, 1997, vol. 76, pp. 103–09.
9. Anon: *Adv. Mater. Process.*, 2006, vol. 164, p. 74.
10. T. Yoneyama, H. Doi, E. Kobayashi, and H. Hamanaka: *J. Mater. Sci.: Mater. Med.*, 2002, vol. 13, pp. 947–51.
11. P. Sevilla, F. Martorell, C. Libenson, J.A. Planell, and F.J. Gil: *J. Mater. Sci.: Mater. Med.*, 2008, vol. 19, pp. 525–29.
12. P. Schloßmacher, T. Hass, and A. Schüßler: *Proc. SMST*, Pacific Grove, CA, 1994, pp. 137–42.
13. A. Tuissi, S. Besseghini, T. Ranucci, F. Squatrito, and M. Pozzi: *Mater. Sci. Eng. A*, 1999, vols. 273–275, pp. 813–17.
14. K. Uenishi, M. Takatugu, M. Seki, T. Kunimasa, K.F. Kobayashi, T. Ikeda, and A. Tuboi: *Mater. Trans.*, 2002, vol. 43, pp. 57–62.
15. A. Falvo, F.M. Furgiuele, and C. Maletta: *Mater. Sci. Eng. A*, 2005, vol. 412, pp. 235–40.
16. X.J. Yan, D.Z. Yang, and M. Qi: *Mater. Charact.*, 2006, vol. 57, pp. 58–63.
17. Y.G. Song, W.S. Li, L. Li, and Y.F. Zheng: *Mater. Lett.*, 2008, vol. 62, pp. 2325–28.
18. H. Gugel, A. Schuermann, and W. Theisen: *Mater. Sci. Eng. A*, 2008, vols. 481–482, pp. 668–71.
19. C. Dawes: *Laser Welding*, McGraw-Hill, New York, NY, 1992, pp. 1–15.
20. S. Kou: *Welding Metallurgy*, John Wiley & Sons, Hoboken, NJ, 2002, pp. 206–09.
21. K. Otsuka and C.M. Wayman: *Shape Memory Materials*, Cambridge University Press, Cambridge, United Kingdom, 1998, pp. 50–62.
22. W. Tang, B. Sundman, R. Sandstrom, and C. Qiu: *Acta Mater.*, 1999, vol. 47, pp. 3457–68.
23. E. Hornbogen, V. Mertinger, and D. Wurzel: *Scripta Mater.*, 2001, vol. 44, pp. 171–78.
24. J. Khalil Allafi, X. Ren, and G. Eggeler: *Acta Mater.*, 2002, vol. 50, pp. 793–803.
25. T. Sawaguchi, G. Kaustrater, A. Yawny, M. Wagner, and G. Eggeler: *Metall. Mater. Trans. A*, 2003, vol. 34A, pp. 2847–59.
26. K.W.K. Yeung, K.M.C. Cheung, W.W. Liu, and C.Y. Chung: *Mater. Sci. Eng. A*, 2004, vol. 383, pp. 213–18.
27. J. Frenzel, E.P. George, A. Dlouhy, C. Somsen, M. Wagner, and G. Eggeler: *Acta Mater.*, 2010, vol. 58, pp. 3444–58.
28. Y. Ogata, M. Takatugu, T. Kunimasa, K. Uenishi, and K.F. Kobayashi: *Mater. Trans.*, 2004, vol. 45 (4), pp. 1070–76.
29. D.L. Shi: *Introduction to Biomaterials*, World Scientific Publishing, Singapore, 2006, pp. 117–36.